

A Ruthenium-Based Multimetal-Contact RF MEMS Switch With a Corrugated Diaphragm

Feixiang Ke, Jianmin Miao, *Member, IEEE*, and Joachim Oberhammer, *Member, IEEE*

Abstract—This paper presents a ruthenium metal-contact RF microelectromechanical system switch based on a corrugated silicon oxide/silicon nitride diaphragm. The corrugations are designed to substantially reduce the influence of the fabrication-induced stress in the membrane, resulting in a highly insensitive design to process parameter variations. Furthermore, a novel multilayer metal-contact concept, comprising a 50-nm chromium/50-nm ruthenium/500-nm gold/50-nm ruthenium structure, is introduced to improve the contact reliability by having a hard-metal surface of ruthenium without substantial compromise in the contact and transmission-line resistances, which is shown by theoretical analysis of the contact physics and confirmed by measurement results. The contact resistance of the novel metallization stack is investigated for different contact pressures and is compared to pure-gold contacts. The contact reliability is investigated for different dc signal currents. At a measurement current of 1.6 mA, the Ru–Au–Ru contacts have an average lifetime of about 100 million cycles, whereas the Au–Au contacts reach 24 million cycles only. For larger signal currents, the metal contacts have proven to be more robust over the Au–Au contacts by a factor of ten. The measured pull-in voltage is reduced significantly from 61 V for flat diaphragm to 36 V for corrugated diaphragm with the introduction of corrugation. The measured RF isolation with a nominal contact separation of 5 μm is better than -30 dB up to 4 GHz and still -21 dB at 15 GHz, whereas the insertion loss of the fully packaged switch including its transmission line is about -0.7 dB up to 4 GHz and -2.8 dB at 15 GHz. [2007-0271]

Index Terms—Contact metal, contact resistance, corrugated membrane, RF microelectromechanical system (MEMS) switch, wafer-level packaging.

I. INTRODUCTION

MICROELECTROMECHANICAL system switches have been receiving increasing attention in recent years, specifically because of their suitability for RF applications in telecommunication, remote sensing, radar [1], [2], etc. The advantages of MEMS switches over their mechanical and solid-state counterparts, with the latter including FETs or p-i-n diode-based semiconductor switches, are low insertion loss, low power consumption, high isolation, high linearity, and, in particular, the fact that metal-contact MEMS switches show these high-performance criteria over a very large bandwidth

from dc up to tens of gigahertz. Furthermore, due to their fabrication based on highly developed semiconductor clean-room facilities and logistics, a high level of miniaturization, high volume with potentially low-cost fabrication, and a high level of integration with other integrated circuit elements are possible [3]. MEMS switches can be used in a variety of RF applications including tunable matching networks [4], [5], phase shifters [6], [7], resonators [8], [9], and reconfigurable filters and amplifiers [10], [11].

RF MEMS switches are usually categorized by contact method and fall into the following two categories: capacitive switches (metal–insulator–metal) and resistive switches (metal–metal). Metal-to-metal switches, typically inserted into an electrical circuit in a series configuration, utilize physical direct contact of metals and can thus be operated from dc to microwave frequencies. Such metal-contact MEMS switches are typically based on a cantilever, an air bridge, or a membrane movable by a micromachined actuator to establish and break the metal–metal contact. A drawback with regard to metal-contact switches is that they are susceptible to contact stiction if the restoring forces are low. Moreover, typical metal-contact switches are suitable for hot switching¹ only for low-power signals with currents of up to a few tens of milliamperes, primarily due to contact surface degradation (such as arcing), which severely restricts the applications of RF MEMS switches.

However, series MEMS switches have recently been developed for medium-power applications as well. Special switch designs for high-power handling have been proposed in recent years [12]–[16]. Active opening mechanisms [17], including a so-called toggle switch design which relies on a push–pull mechanism [18], are more suitable for high-power applications than those designs entirely relying on passive opening forces [19]. A special metal-contact design employing ball grid array dimples demonstrates RF power handling more than 1 W and achieves hot switching in excess of 100 million cycles [20]. Furthermore, the performance of metal-contact MEMS switches is strongly related to the choice of contact material used, particularly for medium-power applications. In connection with the strength of the actuator used, the metal-contact material determines the ON-state resistance and also current-handling capability. Furthermore, the contact material used influences the contact reliability because of material-dependent contact degradation through mechanical wear, fretting, creep,

¹Cold switching, i.e., removing of the signal current during the switch transition in contrast to hot switching where the contacts are separated with the applied signal, allows for much higher current handling capability in the ON state and is therefore limited in its applications, even though suitable for many circuit reconfiguration tasks.

Manuscript received November 9, 2007; revised April 26, 2008 and August 7, 2008. First published September 30, 2008; current version published December 4, 2008. Subject Editor M. Wong.

F. Ke and J. Miao are with the Micromachines Centre, School of Mechanical and Aerospace Engineering, Nanyang Technological University, Singapore 639798 (e-mail: mjmiao@ntu.edu.sg).

J. Oberhammer is with the Microsystem Technology Laboratory, School of Electrical Engineering, Royal Institute of Technology (KTH), 100 44 Stockholm, Sweden.

Color versions of one or more of the figures in this paper are available online at <http://ieeexplore.ieee.org>.

Digital Object Identifier 10.1109/JMEMS.2008.2004786

arcing, electromigration, localized hardening, etc. [21], [22]. Also, when opening the switch, the material-dependent adhesion forces between the closed contacts determine the risk for permanent contact stiction [23], [24]. Initially, soft gold (Au) [23] and slightly harder gold–nickel (AuNi) alloys [25] were used in RF MEMS switch designs because of their low bulk resistivity, low contact resistance even at small contact forces, and their fabrication compatibility with MEMS fabrication methods. However, soft contact materials also exert large contact adhesion forces which require strong opening forces, and are susceptible to contact wear and contact hardening which affect the contact performance. Therefore, different harder contact materials known from the macroscopic relay manufacturing and designed for much larger contact and opening forces have been studied for their suitability as contact materials in miniaturized and microswitches: copper/tungsten/gold stack (Cu/W/Au) [26], rhodium (Re) [27], tungsten (W), molybdenum (Mo), palladium (Pd) [28], silver/tungsten/rhodium (Ag/W/Re) [29], palladium multilayer structures (Ag/Pd, Au/Ag/Pd, Au/Pd) [30], and Ag/W/CdO [31]. Ruthenium has so far only been employed in macroscopic relays because it requires a high contact force [32]. This paper utilizes a chromium/ruthenium/gold/ruthenium (Cr/Ru/Au/Ru) multilayer stack designed to address the current handling and contact reliability issues, and compares the contact performance to switches of the same design but fabricated with conventional titanium/platinum/gold metal contacts.

The bending of any multilayer structure is susceptible to temperature changes. However, a diaphragm clamped all over its circumference is stiffer and therefore much less susceptible to temperature-induced stress, particularly as compared to single-side-clamped structures [33]. Furthermore, the increased stiffness also reduces vibration and shock-induced deflection. Moreover, the diaphragm structure has an advantage of wafer-scale encapsulation at a very early stage during the fabrication, which is distinct from the typical cantilever or bridge structure. However, one shortcoming of a completely clamped moveable membrane is the possible high residual stress in the film which can lead to undesirable effects such as much higher actuation voltage required, film buckling, or even membrane cracking. This paper utilizes a corrugated structure in the membrane which is designed to increase the tolerance to the fabrication-induced stress and to lower the overall stiffness of the diaphragm.

Another challenging aspect of MEMS switches is the packaging. To enhance lifetime, a full-hermetic package in terms of gas tightness is desired. To avoid contamination of switches and, in particular, of the metal contacts during the postprocessing, the encapsulation of switches should happen in an early state of the fabrication. For this purpose, the switches presented in this paper are assembled and encapsulated on wafer scale in one adhesive bonding process, providing a near-hermetic basic encapsulation [17], [34].

II. SWITCH DESIGN ASPECTS AND OPTIMIZATION

A. Switch Concept Overview

Fig. 1 shows a cross-sectional drawing of the RF MEMS switch concept. The core of the switch is the thin and flex-

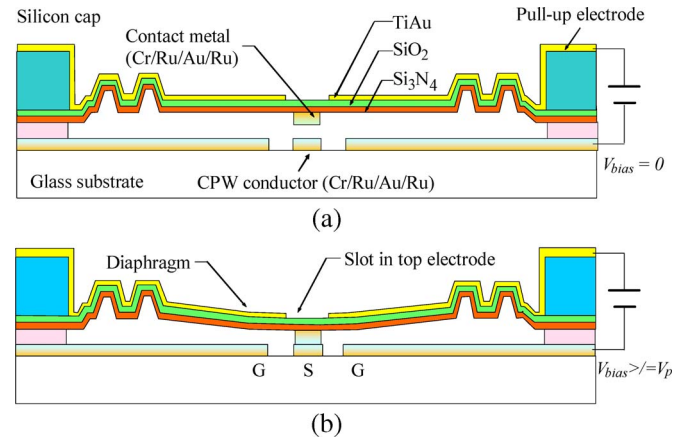


Fig. 1. Cross-sectional drawing of the corrugated-diaphragm-based RF MEMS switch in the (a) OFF and (b) ON states.

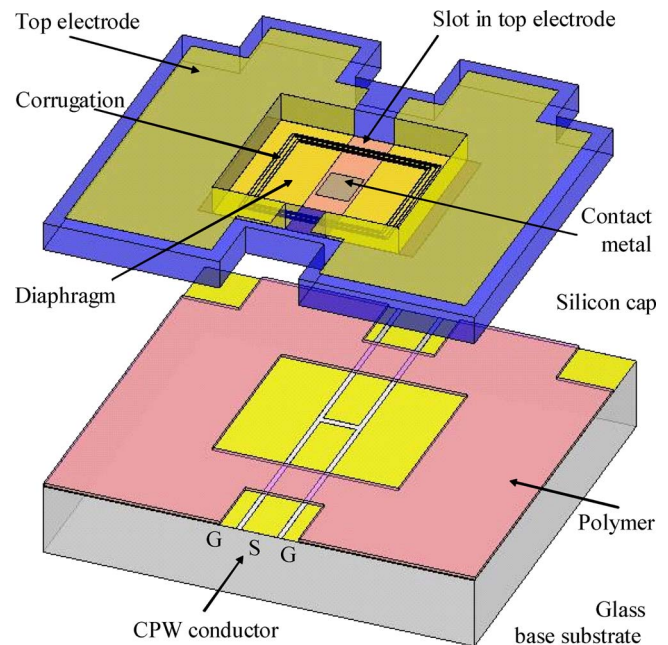


Fig. 2. Schematic drawing of the two switch parts, before assembling by wafer bonding.

ible 100-nm SiO_2 /1200-nm Si_3N_4 diaphragm suspended on polymer distance keepers above the bottom glass substrate. For the switch in the OFF state, this configuration results in a nominal distance of 5 μm between the metal-contact bar on the membrane and the coplanar-waveguide (CPW) signal lines on the bottom wafer. The membrane is actuated by the electrostatic forces between the metal electrodes on the membrane and the electrodes on the bottom wafer. The switch is fabricated in two parts on separate wafers which are finally assembled by bonding with an adhesive polymer ring, as shown in Fig. 2, resulting in a basic encapsulation of the switches on wafer scale. Another advantage of this two-wafer fabrication concept is that it enhances the integration capability of the MEMS switch with other RF circuits or substrates [17]. It means that the moving parts (top silicon with membrane) can be integrated with a large variety of bottom substrates containing RF circuits which may not use fabrication processes compatible with the MEMS moving part.

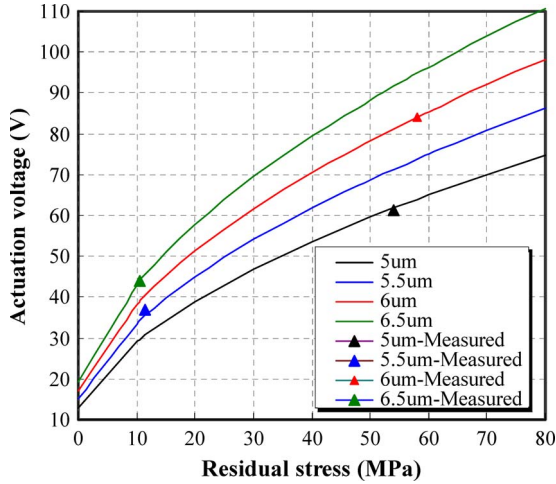


Fig. 3. Actuation voltage versus residual stress of the diaphragm, plotted with the diaphragm suspension height of 5–6.5 μm above the substrate as parameter. The total diaphragm size is $1400 \times 1200 \mu\text{m}$ with a $1080 \times 1200\text{-}\mu\text{m}$ effective electrode area. Measurement results tabulated in Table III are also marked.

B. Stress-Tolerant Design by Corrugations in the Diaphragm

The 100-nm SiO_2 /1200-nm Si_3N_4 film actuator diaphragm has a size of $1400 \times 1200 \times 1.7 \mu\text{m}$, and the top electrodes have a total actuation area of $1080 \times 1200 \mu\text{m}$. For a single-material square diaphragm without corrugations clamped along its circumference, the pull-in voltage V_p for the center part of the diaphragm can be approximated by [35]

$$V_P \approx \frac{64}{7} \sqrt{\frac{Et^3 g_0^3}{5(1-\nu^2)\varepsilon_0 l_a^4} \left(1 + \frac{2}{9}(1-\nu^2) \frac{\sigma l_a^2}{Et^2}\right)} \quad (1)$$

where E , t , ν , l_a , and σ are Young's modulus, thickness, Poisson's ratio, square side length, and residual stress of the diaphragm, respectively, and with g_0 being the nominal suspension height of the diaphragm above the CPW. For the parameters of the present MEMS switch, the relationship of the calculated actuation voltage V_p to the residual stress σ of the diaphragm is shown in Fig. 3 with the nominal suspension g_0 as parameter. To lower the actuation voltage V_p at a given suspension height g_0 (determined by the isolation requirements), the residual stress σ should be minimized. A metal/silicon oxide/silicon nitride diaphragm clamped around its circumference has potentially very high residual stress caused by the different layers by dry oxidation, LPCVD, and sputtering processes, particularly if the metal layer is covering the membrane to a large extent, as in the case of our switch. Large stress in diaphragms can lead to undesirable effects such as very high actuation voltage, as shown in Fig. 3, buckling, or even crack of the diaphragm. A possibility for addressing the stress issue is to reduce the fabrication-induced stress by optimizing the deposition processes. Another effective method to alleviate residual stress in diaphragm and to optimize its mechanical sensitivity is the utilization of corrugation technique [36]–[39]. The application of corrugation offers the possibility to control mechanical sensitivity by means of dimensions of corrugations and the number of corrugations to be used, which is often an easier way compared to the approach by process control.

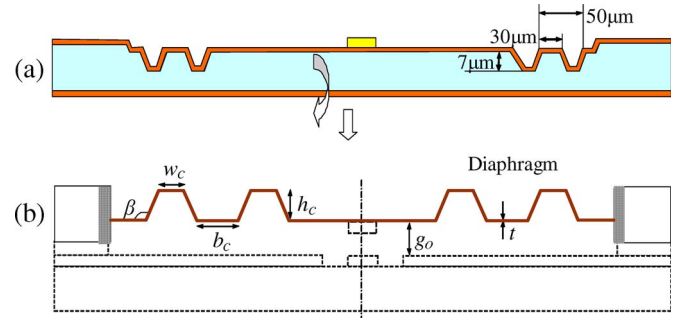


Fig. 4. Geometrical illustration of the corrugations with dimensions. (a) Physical dimensions. (b) Model of the corrugated diaphragm for the numerical simulations and analytical calculations.

Furthermore, the corrugation approach increases the design robustness since it is much more tolerant to deviations in the fabrication-induced stress levels of the different layers, and thus does not require frequent fine-tuning of the process parameters. The corrugation geometry used for the MEMS switch is shown in Fig. 4. The grooves for the corrugations were generated into the silicon wafer either by deep reactive-ion etching (DRIE) or by wet etching using potassium hydroxide (KOH). It is necessary to control the slope of trench wall by DRIE, with a preferable angle of about 85° , to guarantee for good sidewall coverage of the subsequent metal-layer deposition, while the etch profile angle is fixed at 54.7° by wet etching in KOH according to the crystal orientation of the (100) silicon substrate.

The intrinsic tensile stress in a corrugated membrane is significantly released by the corrugations in the structure. Several analytical models for designing corrugated diaphragms with residual stress are available [40], [41], [37]. Fuldner *et al.* [42] proposed a new method to derive an analytical model for corrugated diaphragms for silicon microphones. For relatively high stress and shallow corrugations, i.e., corrugations with a depth h_c less than 0.4 times its period ($w_c + b_c$) [43], the increased bending stiffness in the tangential direction can be neglected, and a corrugated membrane with intrinsic stress σ_0 acts like a flat membrane with a reduced stress σ in equilibrium. That means that the compliance of a corrugated diaphragm $C_{\text{corrugated}}$ can approximately have the form

$$C_{\text{corrugated}} \sigma = C_{\text{flat}} \sigma_0 \quad (2)$$

where C_{flat} is the compliance of the flat membrane with an intrinsic stress σ_0 . Referring to the model shown in Fig. 4, the final intrinsic stress reduction by the introduction of corrugated diaphragms can be calculated as

$$\xi = \frac{\sigma_0}{\sigma} = 1 + 6 \sin(\beta) \left(\frac{h_c}{t}\right)^2 \frac{N_c w_c}{R - N_c(w_c + b_c)} \quad (3)$$

where R is the equivalent radius of the diaphragm, t is thickness of the diaphragm, h_c is the corrugation depth, N_c is the number of corrugations, w_c is the width of bottom corrugations, b_c is the width of top corrugations, and β is the profile angle of corrugations (see Fig. 4). For a rectangular diaphragm, the equivalent radius can be calculated by $R = \sqrt{(w_d/l_d)/\pi}$,

TABLE I
PARAMETERS OF THE PROPOSED CORRUGATED RECTANGULAR
DIAPHRAGM (THE BOTTOM WIDTH w_c OF THE CORRUGATIONS
IS DETERMINED BY THE CORRUGATION DEPTH h_c
AND THE PROFILE ANGLE β)

Parameters	Symbol	Values
diaphragm width	w_d	1200 μm
diaphragm length	l_d	1400 μm
equivalent Diaphragm radius	R	732 μm
diaphragm thickness	t	1.7 μm
width of top corrugation	b_c	30 μm
pitch of the corrugations	λ	50 μm
profile angle of corrugation	β	95° (DRIE) 125.3° (KOH)
number of corrugation	N_c	2

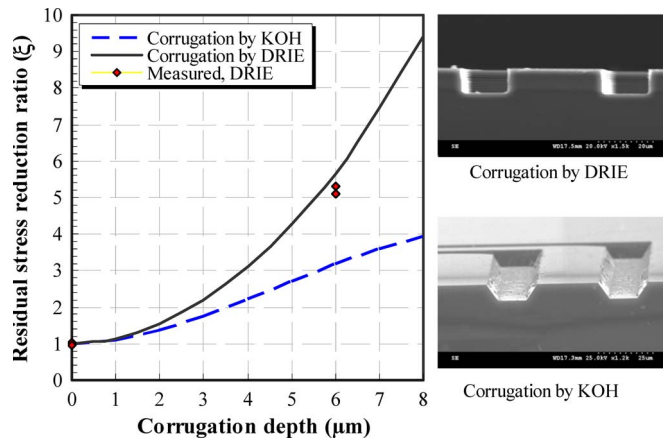


Fig. 5. Residual stress reduction factor (ξ) as a function of the corrugation depth for DRIE- and KOH-etched corrugations (with corrugation number N_c of two). The measured ξ 's given in Table III are also illustrated both for corrugated diaphragms with 6- μm -deep (measured value) corrugations and for flat diaphragm (corrugation depth = 0 μm).

where w_d and l_d are the width and length of the rectangular diaphragm, respectively. The residual stress reduction for the present switch model due to corrugations is calculated using this analytical model with the parameter set listed in Table I. Notice that ξ equals one for a flat diaphragm and is larger than one for a corrugated diaphragm. The calculated stress reduction factors as compared to a flat membrane are shown in Fig. 5 for corrugations etched by KOH with a profile angle of 54.7° ($\beta = 125.3^\circ$) and for corrugations etched by DRIE with a profile angle of 85° ($\beta = 95^\circ$). The stress reduction is significant in both cases and is particularly effective for the DRIE configuration. Thus, DRIE was chosen as the etching technique for the corrugations of the switches presented in this paper.

The footprint area of the present switch design is clearly larger than the footprints of conventional cantilever switches since it is based on a diaphragm structure. Even though the corrugations in the diaphragm reduce its stiffness which allows for designing a much smaller diaphragm without increasing the

actuation voltage, the overall area consumption is still significantly larger as compared to single-side-clamped structures. However, the closed-diaphragm concept, together with the transfer-bonding process, has clear advantages: The switches are encapsulated on wafer level at a very early stage in the fabrication, which makes the devices much less susceptible for contamination and thus eases the handling during subsequent process steps, particularly the packaging of the devices. Furthermore, the transfer bonding has the advantage that much more efficient contact-cleaning procedures might be carried out on both contact surfaces before the bonding, as compared to a fabrication on a single wafer.

C. RF Design

The nominal dimensions of CPW are 250- μm signal-line width and 35- μm gap to the ground lines, resulting in a characteristic impedance of 50.2 Ω for a conductor thickness of 1 μm on a 750- μm -thick Pyrex 7740 glass substrate with a nominal dielectric constant of 4.6. The nominal suspension height of the diaphragm of 5 μm was chosen for a nominal contact distance of 4.35 μm in the OFF state which fulfills the required minimum isolation of -20 dB up to 10 GHz and -15 dB at 30 GHz, determined by RF simulations with ANSOFT HFSS. The isolation is also determined by the overlapping contact area of 250 \times 210 μm which is unexceptionally large for a MEMS switch, designed with the intention of having a large metal volume for an efficient heat sink for the contact-resistance power dissipation to the glass substrate, potentially increasing the current-handling capability. The interruption of the transmission line between the two contacts is 150 μm .

D. Multilayer Contact Metallization Design

This paper introduces a new concept of contact metallization, utilizing a multilayer stack with a covering ruthenium (Ru) layer. Ruthenium has been getting increased attention over palladium, even in macroscopic relay manufacturing, because it offers similar electrical properties and because of the limited availability and drastically increased price of palladium in recent years [44]. Ruthenium, a much harder material as compared to gold-alloy metallization systems, offers the advantages of reduced contact wear, reduced stiction, lower erosion per arcing operation, and better resistance stability but also needs a much stronger actuator for a stable low contact resistance. The metallization multilayer stack utilized in the switches presented in this paper consists of 50-nm chromium/50-nm ruthenium/500-nm gold/50-nm ruthenium (bottom-up, i.e., from the diaphragm to the contact surface) and was applied as contact metallization for the switch contacts both on the moving membrane and on the bottom part (CPW). This multilayer ensures low line resistance of the long CPW and offers, at the same time, the advantages of a hard contact surface, as shown in the following. For comparative measurements, switches with conventional gold metal contacts using 50-nm titanium/100-nm platinum/1000-nm gold have also been fabricated.

The major part of the volume of the proposed metallization stack consists of gold, which gives the metal-contact bar on the moving diaphragm a line resistance close to a pure-gold-contact bar, i.e., much lower as compared to full ruthenium contacts. However, the ruthenium coating results in an increased contact resistance. The total contact resistance R_{CR} is the sum of a constriction resistance term R_c and a film resistance term R_f [45]

$$R_{CR} = R_c + R_f = \frac{\rho}{2a} + \frac{\rho_f d}{\pi a^2} \quad (4)$$

with ρ being the resistivity of the main body of the asperity (contact spot), here gold; a being the radius of the asperity; ρ_f being the resistivity of the film covering the asperity, here ruthenium; and d being the thickness of that film. Typically, multiple asperities are involved in the contact making in microswitches, particularly at low signal currents. In that case, for (4), an equivalent asperity radius can be defined as $\hat{a} = \sqrt{a_1^2 + a_2^2 + \dots + a_n^2}$, with a_1, a_2, \dots, a_n being the asperity radii of the individual contacts [46]. Even for initially multiple-contact points, it has been shown that for signal currents of 1 mA and for soft-gold contacts, one single-contact point begins to dominate over other contact points after a certain number of hot-switching cycles have been carried out [47]. Such reformation of the contact geometry after a relatively low number of hot-switching cycles, based on plastic deformation of the contact surface caused by the actuator's contact force and the power dissipation in the contacts due to the voltage drop over the contacts and the ohmic contact resistance, has also been described as "burn-in behavior" by other authors [48]. For such observations, however, it is difficult to distinguish between the effects of surface cleaning and plastic contact deformation, particularly if the switches are not hermetically packaged and therefore exposed to environmental influences between the fabrication and the tests, which is the case for almost all reports carried out so far.

The effective contact area A_c of the asperity is given by πa^2 , and the relationship between the effective contact area A_c and the contact force is given via the material hardness H by $F = A_c H$ [49]. Thus, in (4), the (equivalent) asperity radius a , which is unknown and difficult to determine, can be expressed and substituted by $a = \sqrt{F/\pi H}$, resulting in

$$R_{CR} = R_c + R_f = \sqrt{\frac{\rho^2 \pi H}{4F}} + \frac{\rho_f d H}{F}. \quad (5)$$

The constriction resistance term R_c in (4) can also be expressed more accurately by taking the mean free path λ of the electrons into account, as given by Nikolic and Allen [50]

$$\hat{R}_C = \gamma(\lambda/a) R_M + R_S = \frac{1 + 0.83(\lambda/a)}{1 + 1.33(\lambda/a)} \frac{\rho}{2a} + \frac{4\rho\lambda}{3\pi a^2} \quad (6)$$

with ρ being the electrical resistivity of the asperity material. The term R_M is called the Maxwell spreading resistance due to lattice scattering, and the term R_S is the Sharvin resistance due to boundary scattering in small constrictions. γ is an interpolation function [47]. The R_S term, in contrast to macroscopic

relays, is of relevant dimension. The total contact resistance based on this equation results to

$$\begin{aligned} \hat{R}_{CR} &= \hat{R}_c + R_f = \gamma(\lambda/a) R_M + R_S + R_f \\ &= \frac{1 + 0.83(\lambda/a)}{1 + 1.33(\lambda/a)} \frac{\rho}{2a} + \frac{4\rho\lambda}{3\pi a^2} + R_f \\ &= \frac{1 + 0.83 \left(\sqrt{\frac{\lambda^2 F}{\pi H}} \right)}{1 + 1.33 \left(\sqrt{\frac{\lambda^2 F}{\pi H}} \right)} \frac{\rho}{2\sqrt{\frac{F}{\pi H}}} + \frac{4\rho\lambda}{3\pi \frac{F}{\pi H}} + \frac{\rho_f d H}{F}. \end{aligned} \quad (7)$$

Fig. 6(a) compares the two calculation methods according to (5) and (7) by using the metal resistivities given in Table II and by plotting the total contact resistance over the contact force. The results of both equations do not differ significantly. Fig. 6(b) shows the total contact resistance depending on the film thickness of the ruthenium coating, as compared to single-material gold contacts and single-material ruthenium contacts. The ruthenium coating increases the total contact resistance as compared to gold-coated gold contacts. Fig. 6(c) shows the relative increase depending on the contact force and the thickness of the coating. Fig. 6 effectively shows the advantages of the proposed contact-coating method. The metallization stack with a 50-nm-thick ruthenium coating on top of gold contacts, as utilized for the fabricated switches in this paper, offers the surface properties of ruthenium contacts, i.e., hardness and durability. The total contact resistance of the novel metallization stack, however, is at least three times smaller as compared with that of pure-ruthenium switch contacts, for typical MEMS microswitch contact forces of 200–400 μ N. Moreover, as compared to the much softer gold contacts with inferior surface durability, the total contact resistance increases by only 1.9–2.5 times for a contact force of 200–400 μ N. It should be noted that the hardness values of ruthenium and gold films for the analysis are obtained by nanoindentation test, a widely used method to determine the hardness and Young's modulus of thin film [51], using a Nanoindenter XP (MTS System Corporation) with a Berkovich tip and a dynamic contact module (DCM). Some 500-nm-thick thin films of pure gold and ruthenium were sputtered on glass wafers for the measurement. Ten indentations were conducted on each sample. The measurement results are as follows: Au-film hardness $H_{Au} = 1.6$ GPa and Ru-film hardness $H_{Ru} = 10.1$ GPa. Additionally, the electron mean free paths of gold and ruthenium used for the analysis are $\lambda_{Au} = 38$ nm [47] and $\lambda_{Ru} = 10.8$ nm [52], respectively.

III. FABRICATION

The fabrication of the diaphragm RF MEMS switch involves surface micromachining and bulk micromachining processes, as well as full-wafer bonding. The fabrication needs seven photolithography masks and one silicon shadow mask. Two of the photolithography masks are used for the processing of the bottom glass wafer, four for the top silicon wafer, and one photolithography mask and a silicon shadow mask for a metal deposition after the wafer bonding. The process flow is shown in Fig. 7.

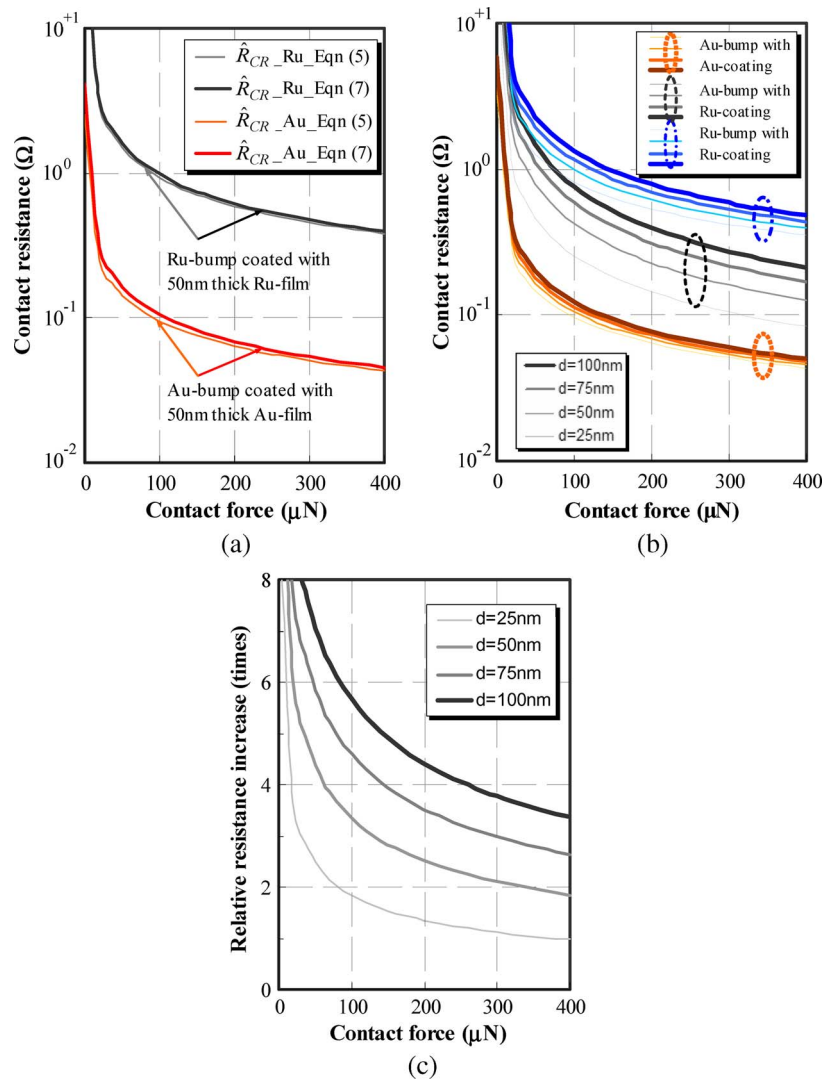


Fig. 6. Analysis of contact resistance over the contact force, for contact bumps coated with coating films. The material parameters for the calculations are in Table II. (a) Comparison of contact resistances calculated by (5) and (7). (b) Total contact resistances of coated contact bumps, with the coating film thickness as parameter. (c) Relative total contact-resistance change of Ru-coated contacts as compared to gold-coated contacts.

TABLE II
PHYSICAL PROPERTIES OF METALS SUITABLE FOR MEMS SWITCH CONTACTS [26]

Item / Material	Ag	Au	Mo	Pd	Pt	Re	Ru	W	Cr
Electrical conductivity ($\text{m}\Omega^{-1} \text{mm}^{-2}$)	63.0	45.7	19.4	9.3	9.5	5.2	14.9	18.0	7.4
Density (g/cm ³)	10.5	19.3	10.2	12.03	21.45	20.90	12.3	19.1	7.19
Melting temperature	960	1063	2620	1555	1774	3170	2450	3400	1857
Boiling temperature	2212	2966	5560	3170	3850	5900	4900	5930	2672
Minimum arc voltage (V)	12.0	12.5	12.0	14.0	14.0	-	-	13.5	-
Minimum arc current (A)	0.4	0.35	0.75	0.80	0.90	-	-	0.8-	-
								1.2	
Price (USD/ounce [26])	4.58	262	5.12	635	603	52.6	141	7.7	-

A. Bottom Glass Wafer

A 750-μm-thick Pyrex glass wafer of 100 mm in diameter was chosen as the substrate material. The CPW was formed on the bottom glass wafer by sputtering a 50-nm Cr/50-nm

Ru/500-nm Au/50-nm Ru metal layer, which is patterned by a lift-off process using AZ 9260 photoresist. Afterward, polymer (CYTOP CTL809M fluoropolymer) is spin coated on the glass wafer with a thickness of 2 μm. The polymer is precured at

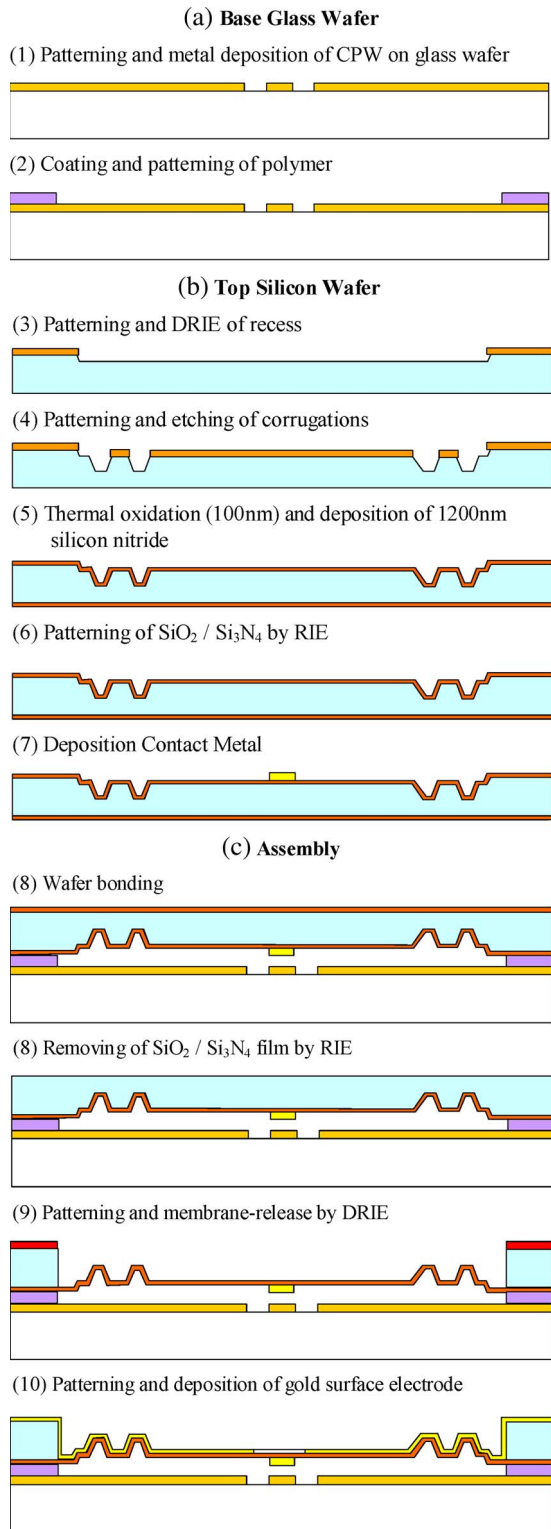


Fig. 7. Fabrication process flow. (a) Bottom glass wafer process. (b) Top silicon wafer process. (c) Wafer bonding and postprocessing.

90 °C for 20 min, followed by a curing step of 100 °C for 30 min, according to a pretreatment recipe developed by our group. The polymer is subsequently patterned by oxygen plasma in a reactive-ion etcher (RIE) with an AZ 9260 photoresist mask of 5 μm .

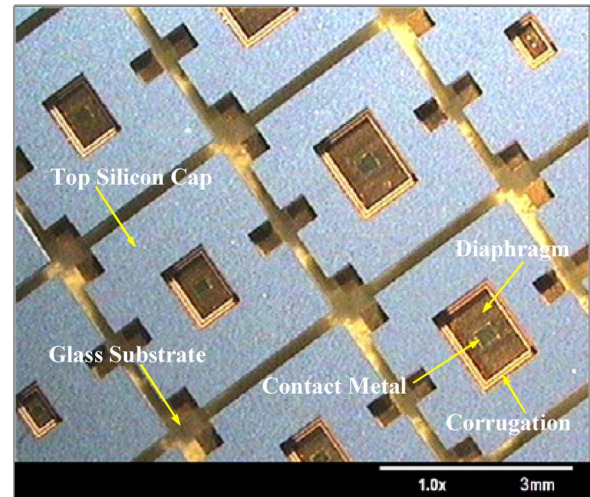


Fig. 8. Photograph of a wafer-scale-packaged RF MEMS switches with a $1400 \times 1200 \times 1.7\text{-}\mu\text{m}$ corrugated diaphragm, before the wafer dicing. The overall size of a single switch after dicing is $3 \times 2.8 \times 0.95\text{ mm}$.

B. Top Silicon Wafer

A rectangular recess is first etched in the 200- μm -thick top silicon wafer. The 3- μm -deep recess, together with the polymer bonding layer and the contact metallization layers, determines the nominal contact separation in the OFF state. The recess is etched by DRIE using a photoresist mask. Afterward, the 8- μm -deep corrugation trenches are created by DRIE. The control of the etching profile angle, preferably close to 85°, is important to have a good sidewall coverage of the final membrane electrode of gold film by sputtering. The desired profile angle is generated in our STS DRIE tool with 8-s etching time and 5-s passivation time at 100-W platen power. The structural layers of the diaphragm are then formed by growing a 100-nm-thick silicon dioxide layer by dry thermal oxidation, followed by an LPCVD deposition of silicon nitride with a thickness of 1200 nm. The compressively stressed thermal silicon dioxide layer is used as a base layer to compensate the tensile stress of silicon nitride to a large extent. The residual stress of silicon nitride film highly depends on the process conditions, particularly on the gas ratios of DCS (SiCl_2H_2) and ammonia (NH_3). The 1200-nm silicon nitride film deposited by a gas ratio of 6:1 (DCS: NH_3) at 850 °C results in a tensile stress of 40 MPa. The $\text{SiO}_2/\text{Si}_3\text{N}_4$ film is patterned afterward by RIE in a CF_4/O_2 plasma, using a photoresist mask. Finally, the contact metal for the metal contacts is created by sputtering a 50-nm Cr/50-nm Ru/500-nm Au/50-nm Ru multilayer patterned by a lift-off process with AZ9260 photoresist. The lift-off resist is subsequently dissolved in acetone. Other than cleaning in isopropanol and DI water, no further cleaning step was undertaken.

C. Wafer Bonding and Postprocessing

The two processed wafers are bonded by using the intermediate adhesive CYTOP polymer layer processed on the bottom wafer in a wafer bonder Karl Suss SB6 at 160 °C with a chuck pressure of 2 bar for 60 min. After the wafer bonding, the $\text{SiO}_2/\text{Si}_3\text{N}_4$ film on the backside of the top wafer is removed by RIE in CF_4/O_2 plasma. The diaphragm release is done by

TABLE III
MEASURED AND CALCULATED PULL-IN VOLTAGE, RESIDUAL STRESS, AND STRESS REDUCTION RATIO FACTOR

	Flat diaphragm		Corrugated diaphragm (with 2 DRIE corrugations)	
	Wafer1	Wafer2	Wafer3	Wafer4
Suspension height g_0 (μm)	5	6	5.5	6.5
Calculated pull-in volta (V)	62.1	82.7	34.5	43.1
Measured pull-in volta (V)	61	84	36	44
Intrinsic stress σ_0 (MPa)	56	56	56	56
Equivalent reduced stress σ (MPa)	54	58	11.0	10.5
Calculated ξ (σ_0/σ)	1	1	5.7	5.7
Measured ξ (σ_0/σ)	1.04	0.97	5.1	5.3

DRIE using a 7- μm -thick AZ 9260 photoresist mask. Finally, a 10-nm Ti/400-nm gold layer is sputtered on the wafer stack to create the membrane electrode. A 200- μm -thick silicon shadow mask, created by DRIE, is used in this process to create the pattern of the top electrodes on the diaphragm and to mask out the areas of the exposed bottom wafer. The shadow mask is placed directly onto the wafer stack by manual alignment under a microscope. Fig. 8 shows a photograph of the fabricated RF MEMS switches before dicing the wafers. The overall size of the dies is much larger than the packaged switch and has the dimensions of $3 \times 2.8 \times 0.95$ mm.

IV. CHARACTERIZATION AND DISCUSSION

The 100-nm SiO_2 /1200-nm Si_3N_4 /400-nm Au film results in an overall residual tensile stress of 56 MPa at wafer level measured by a Tencor surface profilometer, determined by the wafer curvature before and after depositing the films.

Furthermore, the current-handling capacity of the transmission line alone, consisting of the 50-nm Cr/50-nm Ru/500-nm Au/50-nm Ru metallization stack, was investigated in a separated study. A signal line of 3000 μm long, 125 μm wide, and 1.2 μm thick was fabricated on a 750- μm -thick glass which has much lower thermal conductivity than silicon. The maximum dc current-handling capacity of this line can achieve as high as 6.6 A, which corresponds to a current density of 44 $\text{mA}/\mu\text{m}^2$ by consideration of the cross-sectional area of the signal line, without significant degradation observed after several tests. The measured electrical resistance of the line was relatively stable within 5% variation of increment even tested for 24 h at a lower dc current of 0.5 A, corresponding to a current density of 3.3 $\text{mA}/\mu\text{m}^2$.

The pull-in voltage of the MEMS switch was measured, as listed in Table III, together with the measured pull-in voltage for MEMS switch with flat diaphragm for comparison. The pull-in voltage is reduced significantly from 61 V for the flat diaphragm of 5 μm of suspension height to 36 V for the corrugated diaphragms with even higher suspension of 5.5 μm , thanks to the introduction of corrugation structure in the diaphragm. Notice that the equivalent diaphragm stress is only about 11 MPa, which is five times reduced from the intrinsic

stress of 56 MPa. The measured suspension height of the diaphragm was obtained using a Dektak 3ST surface profiler with a stylus force of 5 μN .

The dc single-contact resistance of the MEMS switches was measured by four-probe measurement during subsequent switching cycles, subtracting the line resistance of the contact bar between the two contact points. A measurement current of 1.6 mA was applied for 10 s during each cycle. Ten devices chosen from two wafers were tested (one wafer with Au–Au metal contacts and another wafer with Au/Ru–Ru/Au metal contacts). Fig. 9(a) shows the measured contact resistance of a single Au/Ru–Ru/Au contact plotted over the first 30 switch cycles of five assembled switches actuated at different actuation voltage levels. Here, Au/Ru or Ru/Au refers to the Cr/Ru/Au/Ru multilayer metallization system. For comparison, the measured data of single Au–Au contacts are shown in Fig. 9(b). As expected, higher actuation voltage creates a larger contact force resulting in lower contact resistance. Specifically for Ru, the contact surfaces have to adapt to each other during the first switching cycles until the contact resistance is stabilized. At low contact forces (actuation voltage of less than 60 V for Au/Ru–Ru/Au contacts and less than 40 V for Au–Au contacts), the resistance of the first cycles is very unstable. The Au/Ru–Ru/Au contacts require an actuation voltage of 80 V to result in a stable contact resistance of 730 m Ω , whereas an actuation voltage of 40 V is sufficient for a contact resistance of less than 700 m Ω for Au–Au contacts. This indicates that Au/Ru–Ru/Au contacts require a force that is at least four times larger than for Au–Au contacts. An actuation voltage of 80 V results in a contact resistance of about 300 m Ω for the pure Au–Au contacts. The contact resistance of the novel ruthenium multimetal contacts is much lower as compared with that of pure-ruthenium contacts in the literature, and our contact-resistance measurement confirms the theoretically predicted contact-resistance increase for the chosen metal stack very well. For both metallization types, the variation in the contact resistance among different devices is less than 10% after an initial “burn-in” phase of the contacts about 30 switching cycles, as shown in Fig. 9(a) and (b). Furthermore, the contact surfaces, prior to measurement cycles, have been inspected by X-ray photoelectron spectroscopy (XPS), as shown in Fig. 10. In particular, the Ru sample shows

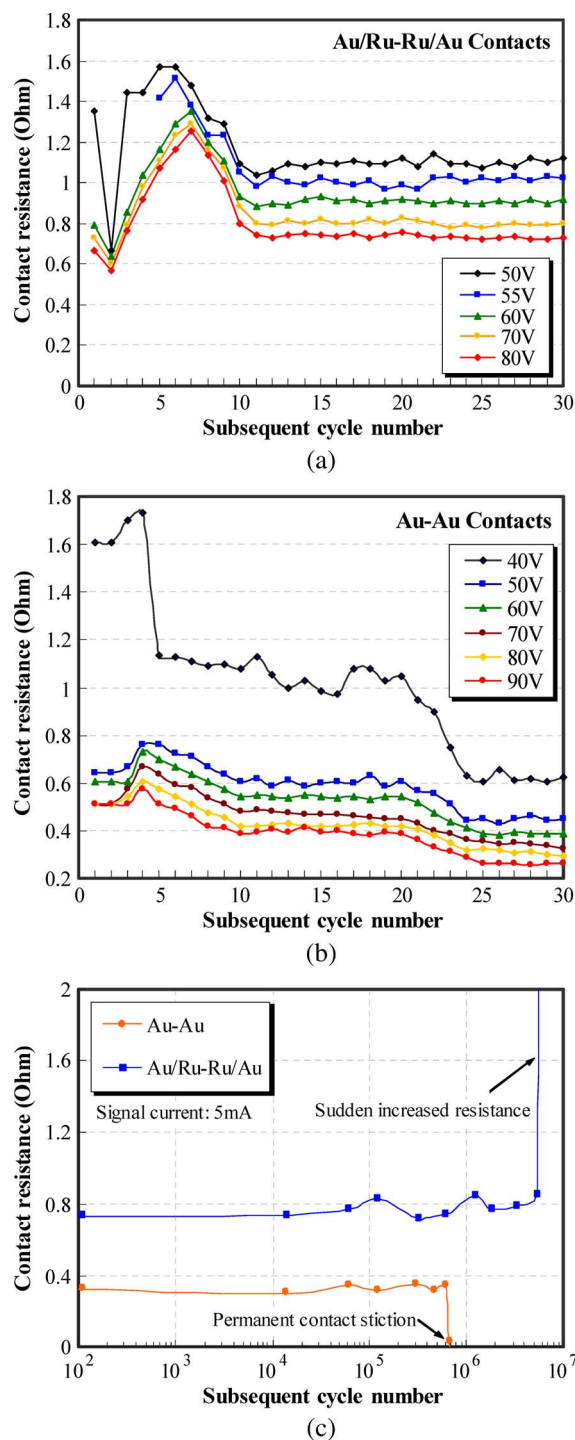


Fig. 9. Contact resistance over switching cycles. (a) First 30 cycles of Au/Ru-Ru/Au contact at different voltage levels. (b) Initial 30 cycles of Au-Au contact at different voltage levels. (c) Contact-resistance change behavior over cycle number with signal current of 5 mA; the resistances and failure points plotted are average values of the two types of devices tested at 5 mA.

carbon peaks in the C1s region. These species are the surface contamination from adsorbed gases, which is a further explanation of the switches requiring a few cycles with applied signal current to locally clean the asperities from surface contaminants before a stable and lower contact resistance is established.

The reliability of the Au/Ru-Ru/Au switch contacts as compared to the Au-Au contacts was investigated in terms

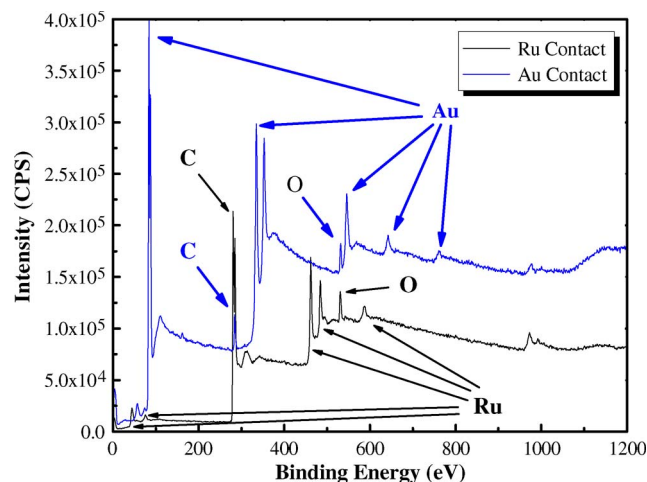


Fig. 10. XPS of the Ru and Au contact surfaces, indicating the presence of absorbed carbon and oxygen on the contact surfaces.

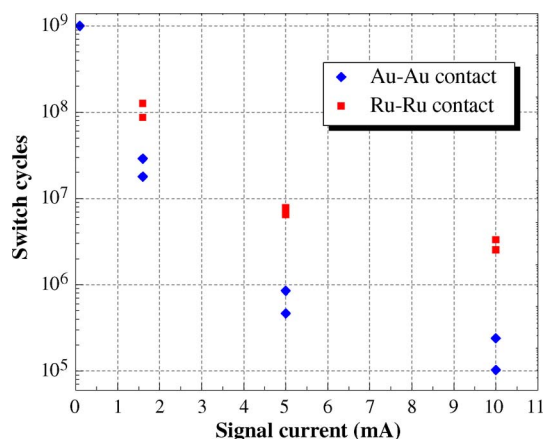


Fig. 11. Contact reliability for the Au-Au and Au/Ru-Ru/Au contacts, investigated for different signal currents. Measurement conditions: cycle frequency of 1 kHz, duty cycle of 20%, and rectangular and monopolar waveforms of 40-V peak amplitude.

of switch-cycle measurements. A square-shaped waveform of 1 kHz with a duty cycle of 20% and a unipolar amplitude of 40 V, on top of a dc offset of 40 V for the Au/Ru-Ru/Au switches and 30 V for the Au-Au switches, was applied to the switch actuator and monitored by an oscilloscope, together with the current in the switched transmission line, as shown in Fig. 12. The reliability of the two different contact metalizations was investigated at different signal currents, and the results are listed in Table IV and shown in Fig. 11. Two wafers were tested, one for Au-Au metal contacts and the other for Au/Ru-Ru/Au metal contacts. Two devices were measured for each current level of 1.6, 5, and 10 mA, respectively. One device with Au-Au metal contact was also tested at 0.1 mA. The measurements show that Au-Au contacts work well for signal currents below 1 mA, achieving over one billion switching cycles before the tests were stopped. At current levels above 1 mA, however, the switches fail prematurely. The durability of the Au/Ru-Ru/Au contacts is higher by a factor of about four times at current level of 1.6 mA and about ten times at current levels of more than 5 mA, as compared to the Au-Au contacts. All of the Au-Au switches failed due to contact

TABLE IV
METAL-CONTACT RELIABILITY IN NUMBER OF SWITCH CYCLES, TWO MEASUREMENT SERIES EACH CARRIED OUT FOR AU-AU AND AU/RU-RU/AU, MEASURED FOR DIFFERENT SIGNAL CURRENTS

Signal current (mA)		0.1	1.6	5	10
Switch cycles, Au-Au contacts (million)	Series 1, Au	>1000 (test stopped)	28.90	0.85	0.24
	Series 2, Au	not measured	18.0	0.47	0.103
Switch cycles, Au/Ru-Ru/Au contact (million)	Series 1, Ru	not measured	126.0	7.80	3.30
	Series 2, Ru	not measured	87.0	6.51	2.53

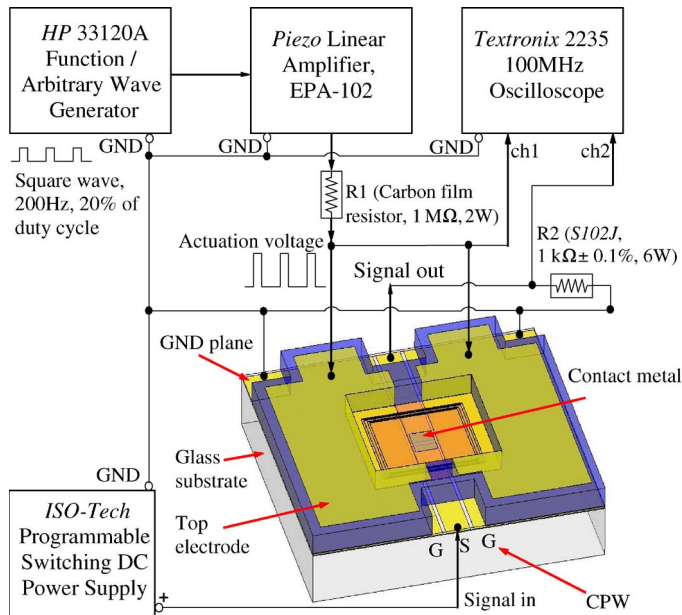


Fig. 12. Schematic diagram of testing setup configuration for the switching-cycle measurement.

welding, observed by irreversible contact stiction. The observed failure mode of the Au/Ru–Ru/Au switches was either due to contact stiction (for 1.6 mA) or a sudden increased resistance above 100 Ω (for 5 and 10 mA). The contact resistances were measured during the lifetime tests, without any obvious contact resistance changes (less than 20% of change) before sudden contact stiction or sudden increased resistance occurred (see Fig. 9(c) showing the case of 5 mA). This is not surprising since ruthenium is a material that is much harder than gold. The gold asperities on the contact surface are much more easily deformed and weld easier together due to the much lower hardness of gold as compared to ruthenium.

The switch-on time was determined, by the same setup of switch-cycle measurement shown in Fig. 12, to be 176 μ s compared with a switching time of 198.5 μ s calculated by the equations given by Steeneken [53]. A square-shaped waveform of 200 Hz with a duty cycle of 20% and an amplitude of 30% higher than the pull-in voltage was applied to the actuator, and the switch-on time was measured by an oscilloscope. It should be pointed out that the current switch design with a wafer-level-encapsulated membrane suffers from squeeze-film damping leading to these long switching times, which are by a factor of four to ten times slower than the switching times of typical

electrostatically actuated cantilever switches. This, however, does not necessarily limit the application fields of the proposed switch design. For some switching applications, such as radar signal encoding, MEMS switches are too slow anyway since switching times of nanoseconds are required. In contrast to that, for many applications, such as the automated reconfiguration of telecommunication networks [54], an application which has attracted increased attention of the RF MEMS community, any MEMS switch with subsecond switching time is fast enough. Also, it should be noted that the switching time of the present switch concept is still by a factor of ten times faster than electrothermally actuated MEMS switches.

The RF performance of the prototypes was measured by using an HP 8722D network analyzer using GSG microwave probe. The measurement results of isolation and insertion loss of the whole chip, i.e., the packaged switch and the 3-mm-long CPW, are shown in Fig. 13, together with the simulation results. The measurement results of the isolation S_{21} for a MEMS switch with 5 μ m of nominal suspension height and a nominal contact distance of 4.35 μ m between the overlapping 250×210 - μ m large contact areas match the simulation results very well over a large frequency range. Up to 1 GHz, the measured isolation is better than -45 dB and, at 15 GHz, the isolation is still better than -20 dB.

The measured insertion loss of the switch including a 3-mm-long transmission line on the silicon substrate is about -0.7 dB up to 4 GHz and -2.8 dB at 15 GHz. These values, however, are worse than the simulation results using the nominal design values, as shown in Fig. 13(b), and are also much worse than typical MEMS switch insertion losses [55]. This discrepancy was investigated, and it was found that the higher insertion loss is mainly caused by the fabrication inaccuracy of the slot in the top-electrode metal layer above the signal line (see Fig. 1). This opening is generated by a shadow mask utilized during the sputtering process, and the nominal width of the opening in the shadow mask is 320 μ m, 70 μ m wider than the center signal line. However, the actual width of the fabricated opening is about 280 μ m, i.e., much narrower than the nominal 320 μ m. The reason for the decreased opening in the electrode metal layer is that the shadow mask is placed at a vertical distance of 200 μ m above the diaphragm during the sputtering, which results in very unsharp edges of the metal pattern. The too narrow slot generates too much reflected power, as shown in Fig. 13. Simulations by Ansoft HFSS Version 9.2 show that the insertion and return losses drastically improve when the open slot in the metal electrode layer changes from 280 to

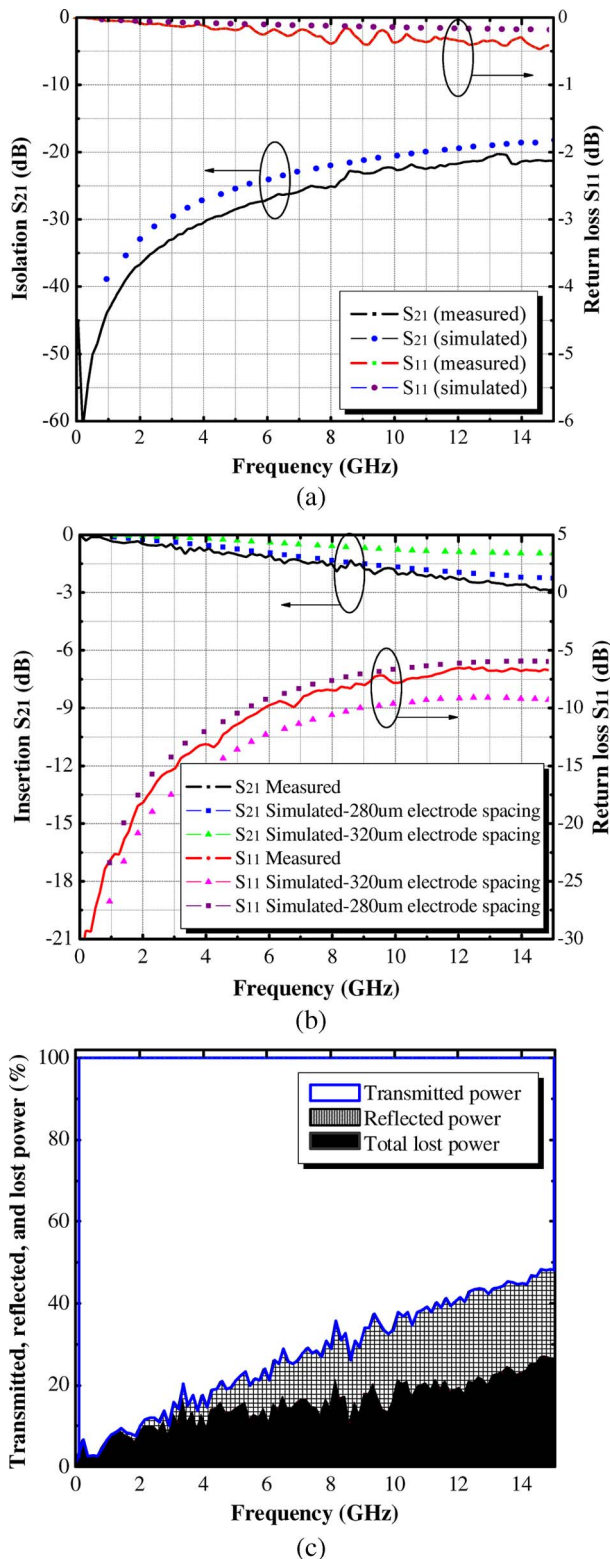


Fig. 13. RF performance of an encapsulated switch including a 3-mm-long CPW transmission line. (a) Simulated and measured S_{21} and S_{11} in the OFF state. (b) Simulated and measured S_{21} and S_{11} in the ON state. The electrode spacing refers to the gap that is left open in the membrane metallization layer. (c) Share percentage of transmitted, reflected, and total lost power.

320 μm [Fig. 13(b)]. However, even for the nominal 320- μm slot in the top metal electrode, the simulated return loss is relatively high as shown in the figure, which is the result of

a general mismatch of the transmission-line design to the 50- Ω measurement setup. Also, the radiation and material losses of the fabricated switches with their 3-mm-long transmission-line piece are relatively high. Fig. 13(c) shows the share of the transmitted-, reflected-, and total-power losses (radiated and dissipated) of the switch plotted in the evaluated spectrum. Approximately 2% of the power losses is contributed by the metal contacts, and the remaining part is by dielectric, radiation and other ohmic losses. For the shadow-mask patterning inaccuracy of the top electrodes, it should be mentioned that the vertical distance of the shadow mask to the diaphragm could drastically be reduced by involving a CMP process step to thin down the top silicon handle wafer before the release of the diaphragm.

The RF measurements are very well reproducible, and five different devices of the same design, obtained from the same fabricated wafer, were evaluated with very well matching results.

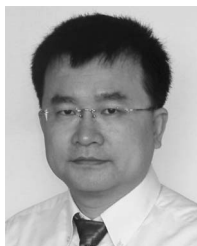
V. CONCLUSION

A novel RF MEMS series metal-contact switch based on a corrugated diaphragm was presented in this paper. The switch employs corrugations in the diaphragm to result in a design that is less sensitive to residual stress in the membrane. The switch is fabricated in two components on two separate wafers which are subsequently bonded by polymer wafer bonding, resulting in a near-hermetic encapsulated switch on wafer level. Furthermore, a new concept for the contact metallization utilizing a multilayer metal stack with a final ruthenium cladding is presented, which combines the advantages of a low-resistivity core of gold with a harder surface coating of ruthenium. The performance of the contact metallization has been analyzed theoretically and confirmed by the measurements. Furthermore, the greater robustness of the ruthenium metal-contact coating could successfully be proven by reliability measurements, compared to switches of the same design with pure-gold contacts. The RF isolation of the switch corresponds very well to the simulation results, but the insertion loss is worse, which was shown to be attributed by an inaccurate shadow-mask sputtering process.

REFERENCES

- [1] H. J. De Los Santos, J. Hector, G. Fischer, H. A. C. Tilmans, and J. T. M. van Beek, "RF MEMS for ubiquitous wireless connectivity. Part I. Fabrication," *IEEE Microw. Mag.*, vol. 5, no. 4, pp. 36–49, Dec. 2004.
- [2] C. T.-C. Nguyen, "Vibrating RF MEMS for low power wireless communications (invited)," in *Proc. IMEMS Workshop*, Singapore, Jul. 4–6, 2001, pp. 21–34.
- [3] G. M. Rebeiz and J. B. Muldavin, "RF MEMS switches and switch circuits," *IEEE Microw. Mag.*, vol. 2, no. 4, pp. 59–71, Dec. 2001.
- [4] T. Vaha-Heikkilä and G. M. Rebeiz, "A 4–18-GHz reconfigurable RF MEMS matching network for power amplifier applications," *Int. J. RF Microw. Comput.-Aided Eng.*, vol. 14, no. 4, pp. 356–372, Jul. 2004.
- [5] Q. Shen and N. S. Barker, "Distributed MEMS tunable matching network using minimal-contact RF-MEMS varactors," *IEEE Trans. Microw. Theory Tech.*, vol. 5, no. 6, pp. 2646–2658, Jun. 2006.
- [6] G. L. Tan, R. E. Mihailovich, J. B. Hacker, J. F. DeNatale, and G. M. Rebeiz, "A 2-bit miniature X-band MEMS phase shifter," *IEEE Microw. Wireless Compon. Lett.*, vol. 13, no. 4, pp. 146–148, Apr. 2003.

- [7] S. Barker and G. M. Rebeiz, "Distributed MEMS true-time delay phase shifters and wideband switches," *IEEE Trans. Microw. Theory Tech.*, vol. 46, no. 11, pp. 1881–1890, Nov. 1998.
- [8] A. R. Brown, P. Blondy, and G. M. Rebeiz, "Microwave and millimeter-wave high- Q micromachined resonators," *Int. J. RF Microw. Comput.-Aided Eng.*, vol. 9, no. 4, pp. 326–337, Jul. 1999.
- [9] F. Torres *et al.*, "Nanometer scale gaps for capacitive transduction improvement on RF-MEMS resonators," *Microelectron. Eng.*, vol. 84, no. 5–8, pp. 1384–1387, May–Aug. 2007.
- [10] J. H. Park, S. Lee, J. M. Kim, H. T. Kim, Y. Kwon, and Y. K. Kim, "Reconfigurable millimeter-wave filters using CPW-based periodic structures with novel multiple-contact MEMS switches," *J. Microelectromech. Syst.*, vol. 14, no. 3, pp. 456–463, Jun. 2005.
- [11] A. Fukuda, H. Okazaki, T. Hirota, and Y. Yamao, "Novel band-reconfigurable high efficiency power amplifier employing RF-MEMS switches," *IEICE Trans. Electron.*, vol. E88-C, no. 11, pp. 2141–2149, Nov. 2005.
- [12] S. Soda, Y. Yoshida, M. Hangai, T. Nishino, S. Izuo, and M. Taguchi, "High power handling capability of movable-waveguide direct contact MEMS switches," in *Proc. 13th Int. Conf. Solid-State Sens., Actuators Microsyst. TRANSDUCERS*, Jun. 5–9, 2005, pp. 1990–1993.
- [13] W. Simon, T. Mack, B. Schauwecker, and K. M. Strohm, "Toggle switch: Investigations of an RF MEMS switch for power applications," *Proc. Inst. Elect. Eng.—Microw., Antennas Propag.*, vol. 152, no. 5, pp. 378–384, Oct. 7, 2005.
- [14] J.-S. Hong, S. G. Tan, Z. Cui, L. Wang, R. B. Greed, and D. C. Voyce, "Development of high power RF MEMS switches," in *Proc. 4th ICMMT*, Aug. 18–21, 2004, pp. 7–10.
- [15] J.-S. Hong, E. P. McErlean, S. G. Tan, Y.-H. Chun, Z. Cui, L. Wang, R. B. Greed, and D. C. Voyce, "Challenge and progress in high power MEMS switches for reconfigurable RF front-ends," in *Proc. IEEE Int. Symp. MAPE Technol. Wireless Commun.*, Aug. 8–12, 2005, vol. 1, pp. 523–526.
- [16] J.-E. Wong, J. H. Lang, and M. A. Schmidt, "An electrostatically-actuated MEMS switch for power applications," in *Proc. 13th Annu. Int. Conf. MEMS*, Jan. 23–27, 2000, pp. 633–638.
- [17] J. Oberhammer and G. Stemme, "Design and fabrication aspects of an S-shaped film actuator based DC to RF MEMS switch," *J. Microelectromech. Syst.*, vol. 13, no. 3, pp. 421–428, Jun. 2004.
- [18] W. Simon, B. Schauwecker, A. Lauer, A. Wien, and I. Wolff, "EM design of broadband RF multiport toggle switches," *Int. J. RF Microw. Comput.-Aided Eng.*, vol. 14, no. 4, pp. 329–337, Jul. 2004.
- [19] J. Oberhammer and G. Stemme, "Active opening force and passive contact force electrostatic switches for soft metal contact materials," *J. Microelectromech. Syst.*, vol. 15, no. 5, pp. 1235–1242, Oct. 2006.
- [20] L. L. W. Chow, J. L. Volakis, K. Saitou, and K. Kurabayashi, "Lifetime extension of RF MEMS direct contact switches in hot switching operations by ball grid array dimple design," *IEEE Electron Device Lett.*, vol. 28, no. 6, pp. 479–481, Jun. 2007.
- [21] R. Holm, *Electric Contacts: Theory and Applications*, 4th ed. Berlin, Germany: Springer-Verlag, 1967.
- [22] M. Braunovic, N. Myshkin, and V. Konchits, *Electrical Contacts: Fundamentals, Applications and Technology*. New York: Taylor & Francis, 2007.
- [23] D. Hyman and M. Mehregany, "Contact physics of gold microcontacts for MEMS switches," *IEEE Trans. Compon. Packag. Technol.*, vol. 22, no. 3, pp. 357–364, Sep. 1999.
- [24] J. Schimkat, "Contact materials for microrelays," in *Proc. 11th Annu. Int. Workshop MEMS*, Jan. 25–29, 1998, pp. 190–194.
- [25] J. Schimkat, "Contact measurement providing basic design data for microrelay actuators," *Sens. Actuators A, Phys.*, vol. 73, no. 1/2, pp. 138–143, Mar. 1999.
- [26] W. Johler, "Precious metal-reduced contact materials in telecom and signal relays," in *Proc. 47th IEEE Holm Conf. Elect. Contacts*, Sep. 10–12, 2001, pp. 104–116.
- [27] T. Umemoto, T. Takeuchi, and R. Tanaka, "The behavior of surface oxide film on ruthenium and rhodium plated contacts," *IEEE Trans. Compon., Hybrids, Manuf. Technol.*, vol. CHMT-1, no. 1, pp. 103–107, Mar. 1978.
- [28] W. Jahn, "Contact metals for reed switches," in *Proc. 36th IEEE Holm Conf., 15th Int. Conf. Elect. Contacts*, Aug. 20–24, 1990, pp. 53–58.
- [29] E. Walczuk, S. Stolarz, and K. Wojtasik, "Experimental study of Ag–W–Re composite materials under high-current conditions," *IEEE Trans. Compon., Hybrids, Manuf. Technol.*, vol. CHMT-10, no. 2, pp. 283–289, Jun. 1987.
- [30] S. Umemura, K. Yasuda, and T. Aoki, "Contact resistance characteristics of noble metal alloys for connector contacts," *IEEE Trans. Compon., Hybrids, Manuf. Technol.*, vol. 14, no. 1, pp. 181–186, Mar. 1991.
- [31] G. S. Paul, "The use of Ag–W–CdO and AgSi₃N₄ as contact materials," *IEEE Trans. Parts, Hybrids, Packag.*, vol. PHP-12, no. 1, pp. 20–24, Mar. 1976.
- [32] J. A. Augis and L. L. Hines, "Sputtered ruthenium as a contact materials for sealed reeds," *IEEE Trans. Compon., Hybrids, Manuf. Technol.*, vol. CHMT-1, no. 1, pp. 46–53, Mar. 1978.
- [33] D. Dubuc *et al.*, "Smart MEMS concept for high secure RF and millimeter-wave communications," *Microelectron. Reliab.*, vol. 44, no. 6, pp. 899–907, Jun. 2004.
- [34] J. Oberhammer, F. Niklaus, and G. Stemme, "Sealing of adhesive bonded devices on wafer-level," *Sens. Actuators A, Phys.*, vol. 110, no. 1–3, pp. 407–412, Feb. 2004.
- [35] P.-C. Hsu, C. H. Mastrangelo, and K. D. Wise, "A high sensitivity polysilicon diaphragm condenser microphone," in *Proc. 11th Annu. Int. Workshop MEMS*, Jan. 25–29, 1998, pp. 580–585.
- [36] J. Miao, R. Lin, L. Chen, Q. Zou, S. Y. Lim, and S. H. Seah, "Design considerations in micromachined silicon microphones," *Microelectron. J.*, vol. 33, no. 1, pp. 21–28, Jan. 2002.
- [37] Q. Zou, Z. J. Li, and L. T. Liu, "Design and fabrication of silicon condenser microphone using corrugated diaphragm technique," *J. Microelectromech. Syst.*, vol. 5, no. 3, pp. 197–204, Sep. 1996.
- [38] Y. Zhang and K. D. Wise, "Performance of non-planar silicon diaphragms under deflections," *J. Microelectromech. Syst.*, vol. 3, no. 2, pp. 59–68, Jun. 1994.
- [39] O. C. Jeong and S. S. Yang, "Fabrication of a thermopneumatic microactuator with a corrugated p+ silicon diaphragm," *Sens. Actuators*, vol. 80, no. 1, pp. 62–67, Mar. 2000.
- [40] P. R. Scheeper, W. Olthuis, and P. Bergveld, "The design, fabrication, and testing of corrugated silicon nitride diaphragms," *J. Microelectromech. Syst.*, vol. 3, no. 1, pp. 36–42, Mar. 1994.
- [41] M. Ying, Q. Zou, and S. Yi, "Finite-element analysis of silicon condenser microphones with corrugated diaphragms," *Finite Elem. Anal. Des.*, vol. 30, no. 1, pp. 163–167, Jul. 1998.
- [42] M. Fuldner, A. Dehe, and R. Lerch, "Analytical analysis and finite element simulation of advanced membranes for silicon microphones," *IEEE Sensors J.*, vol. 5, no. 5, pp. 857–863, Oct. 2005.
- [43] Y. Tang, K. Stanley, J. Wu, D. Ghosh, and J. Zhang, "Design consideration of micro thin film solid-oxide fuel cells," *J. Micromech. Microeng.*, vol. 15, no. 9, pp. 185–192, Aug. 2005.
- [44] W. Johler, "Impact of lead-free soldering processes on the performance of signal relay contacts," *IEEE Trans. Compon. Packag. Technol.*, vol. 27, no. 1, pp. 30–41, Mar. 2004.
- [45] P. G. Slade, *Electrical Contacts Principles and Applications*. Horseheads, NY: Cutler-Hammer, 1999.
- [46] S. Majumder, N. E. McGruer, G. G. Adams, P. M. Zavracky, R. H. Morrison, and J. Krim, "Study of contacts in an electrostatically actuated microswitch," *Sens. Actuators A, Phys.*, vol. 93, no. 1, pp. 19–26, Aug. 2001.
- [47] L. L. W. Chow, S. A. Schrader, and K. Kurabayashi, "Transition from multiple to single microcontact conduction during hot switching of microelectromechanical switches with ball-shaped dimples," *Appl. Phys. Lett.*, vol. 89, no. 13, p. 133 501, Sep. 2006.
- [48] J. Oberhammer, M. Tang, A. Q. Liu, and G. Stemme, "Mechanically tri-stable, true single-pole-double-throw (SPDT) switches," *J. Micromech. Microeng.*, vol. 16, no. 11, pp. 2251–2258, Sep. 2006.
- [49] F. P. Bowden and D. Tabor, *Friction and Lubrication of Solids*, vol. II. London, U.K.: Oxford Univ. Press, 1964.
- [50] B. Nikolic and P. B. Allen, "Electron transport through a circular constriction," *Phys. Rev. B, Condens. Matter*, vol. 60, no. 6, pp. 3963–3969, Aug. 1999.
- [51] L. Chen, H. Lee, Z. J. Guo, N. E. McGruer, K. W. Gilbert, S. Mall, K. D. Leedy, and G. G. Adams, "Contact resistance study of noble metals and alloy films using a scanning probe microscope test station," *J. Appl. Phys.*, vol. 102, no. 7, pp. 074 910–1–074 910–7, Oct. 2007.
- [52] O. H. Blackwood, W. C. Kelly, and R. M. Bell, *General Physics*, 4th ed. Hoboken, NJ: Wiley, 1973.
- [53] P. G. Steeneken, "Dynamics and squeeze film gas damping of a capacitive RF MEMS switch," *J. Micromech. Microeng.*, vol. 15, no. 1, pp. 176–184, Oct. 2005.
- [54] S. Braun, J. Oberhammer, and G. Stemme, "Single-chip MEMS 5 × 5 and 20 × 20 double-pole single-throw switch arrays for automating telecommunication networks," *J. Micromech. Microeng.*, vol. 18, no. 1, p. 015 014, Dec. 1–11, 2007.
- [55] G. M. Rebeiz, *RF MEMS Theory, Design, and Technology*, 1st ed. Hoboken, NJ: Wiley, 2003.



Feixiang Ke received the B.Eng. degree in electronic engineering from Southeast University, Nanjing, China, in 1985, and the M.Sc. degree in electronic engineering from the National University of Singapore, Singapore, in 2000. He is currently working toward the Ph.D. degree in mechanical and aerospace engineering at Nanyang Technological University, Singapore.

He joined DSO National Laboratories, Singapore, in 1993. His research interests include RF MEMS technology and microelectronic packaging.



Jianmin Miao (M'02) received the Dipl.-Ing. and Dr.-Ing. degrees from Darmstadt University of Technology, Darmstadt, Germany, in 1991 and 1996, respectively.

After his MEMS R&D career in industry, in 1998, he joined Nanyang Technological University, Singapore, where he is currently an Associate Professor with the School of Mechanical and Aerospace Engineering. He is the Founding Director of the Micromachines (MEMS) Center and the Director for the Strategic Research Program of MEMS. He is the

author or coauthor of numerous technical papers published in international journals and conference proceedings and the author or coauthor of several books/book chapters. He is the holder of several patents on MEMS. His research interests include MEMS/NEMS design, technology development, biochip fabrication, and nanotechnology.

Prof. Miao has organized and coorganized several MEMS and nanotechnology international conferences and served on the technical committees for international conferences, including IEEE MEMS and TRANSDUCERS.



Joachim Oberhammer (M'06) was born in Italy in 1976. He received the M.Sc. degree in electrical engineering from Graz University of Technology, Graz, Austria, in 2000, and the Ph.D. degree from the Royal Institute of Technology (KTH), Stockholm, Sweden, in 2004, for his work on RF MEMS switches and microsystem packaging.

He was working with automotive sensor electronics and RFID systems with Graz University of Technology and Vienna University of Technology, Vienna, Austria, before he joined the Microsystem

Technology Laboratory, School of Electrical Engineering, KTH. After having been a Postdoctoral Research Fellow with Nanyang Technological University, Singapore, he returned to KTH in 2005, attending an Assistant Professor position and heading a research team with activities in RF MEMS. In 2007, he became an Associate Professor with KTH. In 2007 and 2008, he was a Guest Researcher with Nanyang Technological University and Kyoto University, Kyoto, Japan, respectively. He is the author or coauthor of more than 40 reviewed research papers. He is the holder of three patents.